Electrochimica Acta 255 (2017) 230–238

Contents lists available at ScienceDirect

Electrochimica Acta

journal homepage: www.elsevier.com/locate/electacta

Research Paper

Hydrostatic pressure effects on the kinetic parameters of hydrogen evolution and permeation in Armco iron

X.L. Xiong[a], H.X. Ma[a], X. Tao[a], J.X. Li[a], Y.J. Su[a,*], Q.J. Zhou[b], Alex A. Volinsky[c]

[a] Corrosion and Protection Center, Key Laboratory for Environmental Fracture (MOE), University of Science and Technology Beijing, Beijing 100083, China
[b] Research Institute, Baoshan Iron & Steel Co. Ltd, Shanghai 201900, China
[c] Department of Mechanical Engineering, University of South Florida, Tampa FL 33620, USA

ARTICLE INFO

Article history:
Received 11 July 2017
Received in revised form 22 September 2017
Accepted 28 September 2017
Available online 29 September 2017

Keywords:
Iron
Hydrogen permeation
Hydrostatic absorption

ABSTRACT

Armco iron samples are exposed to pressures of 0.1–30 MPa to study hydrogen permeation during potentiostatic charging. Elecrochemical impedance spectroscopy (EIS) is performed to analyze the electrode/electrolyte interface reaction. According to EIS and first-principles calculations, the hydrostatic pressure decreases the distance between the adsorbed hydrogen atoms and the sample surface, which induces hydrogen atom diffusion into the subsurface by decreasing the diffusion barrier energy. Under high pressure, hydrogen molecules gather at the sample entry side and inhibit the hydrogen recombination reaction. Thus, the amount of adsorbed hydrogen and the hydrogen subsurface coverage increase.

1. Introduction

Deep-sea water can induce severe hydrogen-induced cracking (HIC) of metallic materials and structures [1], which stimulated several studies of the hydrostatic pressure effects on HIC. Olsen et al. demonstrated that the hydrostatic pressure could significantly increase the hydrogen concentration in duplex stainless steels and super martensitic steels when immersed in a 3.5% NaCl electrolyte with aluminum anodes. Thus, HIC occurs more easily in deep-sea environment [2]. Therefore, research of the diffusion and hydrogen evolution reaction (HER) mechanisms in steels under hydrostatic pressure is essential.

Experiments of the pressure effects on hydrogen diffusion mechanisms in metals have been performed by many researchers since 1966. Woodward et al. [3] and Nanis et al. [4] claimed that the hydrostatic pressure increased the permeation rate, but the diffusivity remained unchanged. However, Smirnova et al. [5] and Blundy et al. [6,7] found that the permeation flux was independent from the hydrostatic pressure if the electrolyte was stirred at the entry side. The authors hypothesized that the permeation rate increased with the hydrogen partial pressure at the entry side and that hydrostatic pressure did not directly affect the permeation rate. Based on the surface effect model [8], Xiong et al. experimentally demonstrated that the hydrostatic pressure directly affected the hydrogen surface adsorption. The hydrogen concentration at the subsurface of the A514 steel membrane increased with hydrostatic pressure [9]. However, the effects of the hydrostatic pressure on each kinetic parameter of HER remain unclear.

During the past decade, models of hydrogen permeation have been developed, allowing to obtain kinetic parameters for the HER. These models show that hydrogen diffuses into metal in alkaline solutions in the following reaction [8,10–12]:

$$H_2O + M + e^- \overset{k_1}{} MH_{ads} + OH^- \quad (1)$$

Here, M represents the metal electrode, and MH_{ads} represents a hydrogen atom adsorbed on the metal surface. Parts of the adsorbed hydrogen atoms recombine into a hydrogen molecule via the simple Tafel chemical recombination reaction:

$$MH_{ads} + MH_{ads} \overset{k_2}{} H_2 + 2M \quad (2)$$

or by the Heyrovsky electrochemical reaction:

$$MH_{ads} + H_2O + e^- \overset{k_3}{} H_2 + OH^- + M \quad (3)$$

In alkaline solution, the coupled discharge-chemical desorption occurs at lower overpotential, and slow discharge-fast electrochemical desorption occurs at higher overpotential [12]. Adsorption is followed by absorption of some adsorbed hydrogen atoms.

* Corresponding author.
E-mail address: yjsu@ustb.edu.cn (Y.J. Su).

https://doi.org/10.1016/j.electacta.2017.09.181
0013-4686/

Thus, hydrogen atoms diffuse into the subsurface immediately under the electrode surface as follows:

$$MH_{ads} + M_{subsurface} \leftrightarrow M_{surface} + MH_{abs}(subsurface) \quad (4)$$

Then, the absorbed hydrogen atoms diffuse from the subsurface into the bulk metal:

$$MH_{abs}(subsurface) \rightarrow MH_{abs}(bulk) \quad (5)$$

The absorption of hydrogen into metals shown above is the first and necessary step in hydrogen embrittlement [8,10,13]. Some researchers considered the surface effects at the hydrogen entry side during electrochemical hydrogen permeation [8,14–16]. By measuring kinetic parameters of the HER, one can illustrate the pressure effects on reactions (1) through (5).

To measure kinetic parameters of the HER, general derivation of the Iver-Pickering-Zamenzadeh (IPZ) model [17] was adopted in this paper. This model, proposed by Al-Faqeer et al., is applicable for the discharge-recombination process of hydrogen evolution in electrode/electrolyte systems under the Frumkin and the Langmuir adsorption conditions.

According to the Frumkin adsorption isotherm, the free energy of the species adsorption is correlated with the species coverage as follows:

$$\Delta G_\theta^o = \Delta G_0^o + fRT\theta \quad (6)$$

where ΔG_θ^o and ΔG_0^o are standard free energies of the adsorption at coverage θ and zero coverage (θ=0), respectively; R is the gas constant; T is the absolute temperature; f is a dimensionless factor, which describes the deviation from the ideal Langmuir behavior. The change in ΔG_θ^o is represented by the fRT quantity.

To evaluate kinetic parameters of the HER, Eqs. (7)–(9) were derived based on the original IPZ model [14–16] and the Frumkin adsorption in Eq. (6):

$$\frac{\sqrt{i_r}}{i_\infty} i_c \exp\left(\frac{F\alpha\eta}{RT}\right) = \sqrt{\frac{k_2 i_o'}{F\,k}}\left(1 - \frac{1}{Fk} i_\infty\right) \quad (7)$$

$$\ln\left(\frac{\sqrt{i_r}}{i_\infty}\right) = \ln\left(\sqrt{\frac{k_2}{F\,k}}1\right) + \frac{\alpha f}{Fk} i_\infty \quad (8)$$

$$i_\infty = Fk\theta \quad (9)$$

where i_∞ and i_r are the current densities of the steady-state and adsorbed hydrogen atom combination; i_c is the charging current density; k_2 is the kinetic parameter in Eq. (2); α is the transfer coefficient; F is the Faraday's constant; η is the overpotential ($\eta = E_{applied} - E_{corr}$; $E_{applied}$ is the applied cathodic potential; E_{corr} is the corrosion potential).

$$i_o' = Fk_1 C_{H^+} = i_o/(1 - \theta_H^e) \quad (10)$$

Here, i_o is the exchange current density of the HER; θ_H^e is the hydrogen surface coverage at equilibrium; C_{H^+} is the hydrogen ion concentration in the electrolyte; k is the kinetic diffusion constant, which is defined as

$$k = \frac{k_{abs}}{1 + k_{des}\frac{L}{D}} \quad (11)$$

In Eq. (11), k_{abs} is the rate constant for hydrogen absorption into the metal at the charging surface; k_{des} is the rate constant of hydrogen desorption in the opposite direction, i.e., from the absorbed to the adsorbed state; D is the hydrogen diffusion coefficient in the membrane; L is the membrane thickness. i_∞, i_r and i_c can be obtained from the experimental data. When a suitable $E_{applied}$ for hydrogen charging is chosen, HER follows the coupled discharge-recombination mechanism [12]. Thus, linear relationships between $\sqrt{i_r}/i_\infty i_c \exp(F\alpha\eta/RT)$ and i_∞, and between $\ln\left(\sqrt{i_r}/i_\infty\right)$ and i_∞, can be obtained. The kinetic parameters of the HER can be calculated based on Eqs. (7)–(9).

Since HER occurs at the metal surface/electrolyte interface, it is necessary to provide further insight into the pressure effect on the structure of the double-layer capacitance. The notion of double-layer capacitance was first mentioned by Gouy [18], Chapman [19] and Stern [20]. However, this model did not consider the ion volume and hydrostatic pressure generated by the Coulomb force. Both models proposed by Shapovalov [21] and Dreyer [22] claimed that the electrostatically generated pressure was not negligible; it could be several hundred MPa near the electrode surface and dramatically decrease with the distance from the electrode surface, which proved that the hydrostatic pressure of the electrolyte (approximately 30 MPa) could affect the ion distribution in the double layer. The double-layer thickness can change the place of the HER, so the pressure obviously affects the adsorption and absorption of hydrogen atoms. However, this effect cannot be directly observed. Combined with the EIS analysis results, first-principles calculations based on the density functional theory (DFT) were used to qualitatively explain the effects of the change in double-layer thickness on the HER kinetics under different hydrostatic pressures. Based on the DFT, the hydrogen adsorption and diffusion in metals were simulated in several studies [23–27]. Here, a minimum energy path of hydrogen diffusion into the Fe subsurface was obtained using the well-known climbing nudged elastic-band (CNEB) calculation method [28]. Then, using the Debye model [29], we calculated the Gibbs free energy of each structure in the hydrogen diffusion path, which diffused from the surface adsorption into the (100) Fe subsurface, as obtained by the CNEB. This energy path enables us to relate the energy barrier for hydrogen diffusion into the Fe subsurface and the position for HER. Finally, the hydrostatic pressure effect on the hydrogen diffusion into Fe can be qualitatively described.

This paper analyzes the effects of the hydrostatic pressure on the kinetics of HER and electrode/electrolyte interface based on the electrochemical hydrogen permeation and electrochemical impedance spectroscopy. In addition, the DFT and the Debye models calculations are used to qualitatively explain the pressure effect on hydrogen diffusion into the Fe subsurface.

2. Materials and methods

2.1. Tested materials

Armco iron was used in this work with the following composition in wt%: 0.025 C; 0.006 Mn; 0.01 Mo; 0.001 Si. The permeation and potentiodynamic polarization test samples had a circular shape with 1.2 cm radius and were exposed to the solution. To avoid the edge effects and ensure one-dimensional diffusion, the samples were 0.5 ± 0.01 mm thick. Both sides of the samples were polished and coated with 100 nm of nickel using sputter deposition in an ultra-high vacuum. Sputter deposition was conducted in a thin-film sputtering system (LAD18, KJLC). The samples for EIS tests had a circular shape with 1.2 cm radius and 1 ± 0.01 mm thickness and were polished on both sides.

2.2. High-pressure electrochemical investigation methods

The double-cell electrochemical equipment, which consists of two compartment autoclaves and a hydraulic system, was used to

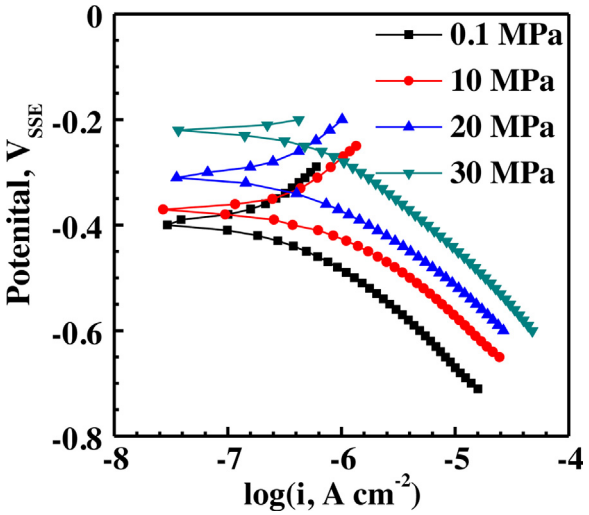

Fig. 1. Potentiodynamic polarization curves for different hydrostatic pressures in 0.2 mol/L NaOH + 0.22 g/L thiourea solution at 25 °C.

perform the hydrogen permeation experiments under various hydrostatic pressures. A three-electrode system was used in each autoclave. A piece of platinum foil with a size of 10 mm × 30 mm was used as the counter electrode, and an Ag/AgCl electrode (SSE) saturated with KCl was used as the reference electrode (+0.197 V vs. the standard hydrogen electrode). Details of the equipment are provided in previous work [9]. Hydrostatic pressures of 0.1, 10, 20 and 30 MPa were applied in two cells. All tests were performed at 25 °C.

Potentiodynamic polarization tests were performed before the hydrogen permeation experiment on the same sample. To protect the sample surface, the potential of the samples was swept at a rate of 0.01 V/s from the initial potential of −0.40 V vs. the open circuit potential (E_{OCP}) to E_{OCP}. The potentiodynamic polarization tests were conducted with 0.2 mol/L NaOH + 0.22 g/L thiourea. Based on the Tafel plot, E_{corr} at each hydrostatic pressure was obtained.

Hydrogen permeation tests were conducted by applying constant $E_{applied}$ to the samples at the hydrogen charging side. These potentials were obtained as the sum of preset η with respect to E_{corr} and E_{corr}. η ranged from −0.66 V to −0.56 V in 0.02 V increments. A positive overpotential of +0.3 V was applied to the sample in the hydrogen oxidation cell. The hydrogen atoms that diffused to the surface of the hydrogen exit side were oxidized; thus, the hydrogen current was obtained. Since the traps in the metal significantly affect the hydrogen diffusivity [30–34], the first hydrogen permeation experiment was performed under atmospheric pressure to fill the hydrogen traps. To release the diffusible hydrogen atoms, all charged specimens were exposed to air for 48 hours. Finally, permeation tests were performed under different hydrostatic pressures with 0.2 mol/L NaOH in the oxidation cell and 0.2 mol/L NaOH+0.22 g/L thiourea in the hydrogen charging cell.

The EIS analysis was performed with a bias of 0.01 V at frequencies of 100 kHz – 10 mHz at different hydrostatic pressures. The applied potentials were the sum of preset η and E_{corr}. η = −0.66 V was applied in the EIS experiments under different hydrostatic pressures. After the current reached a steady state, EIS measurements were performed in 0.2 mol/L NaOH.

2.3. First-principles calculation methods

The first-principles calculations were based on the density functional theory using the Vienna Ab-Initio Simulation Package (VASP) [35,36]. All calculations were performed in the polarized spin. The k-points and cutoff energy of the super-cell were tested. A kinetic cutoff energy of 350 eV was used throughout the convergence tests. The perfect structure of α-Fe with the (100)

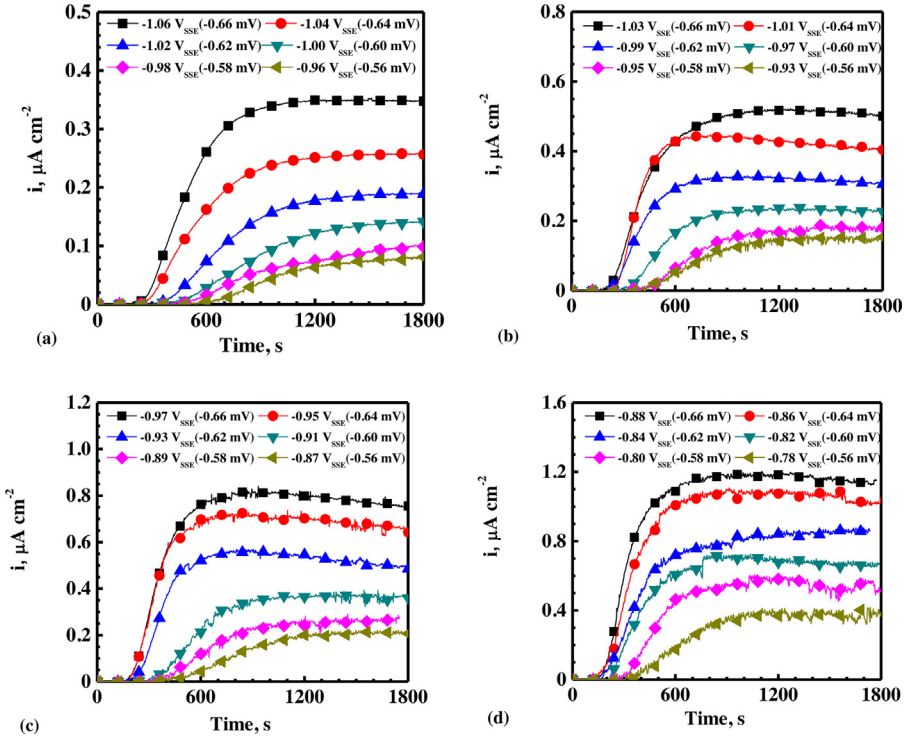

Fig. 2. Permeation curves for different $E_{applied}$ and hydrostatic pressures in 0.2 mol/L NaOH in the oxidation cell and 0.2 mol/L NaOH + 0.22 g/L thiourea in the hydrogen charging cell at 25 °C. The hydrostatic pressure was 0.1–30 MPa in (a)-(d). The overpotentials η with respect to E_{corr} are in the brackets.

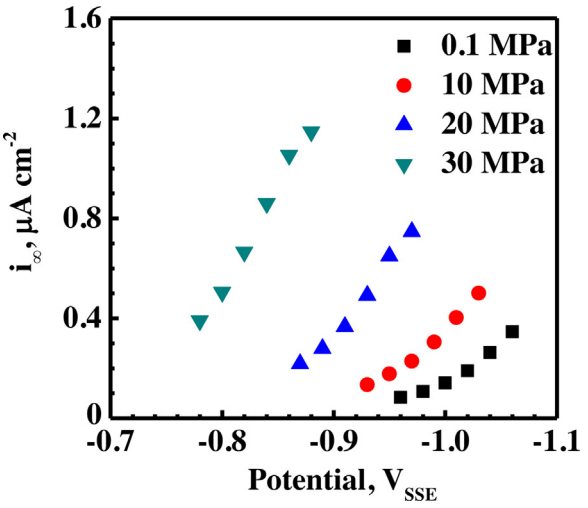

Fig. 3. Dependence of the steady-state current density, on the hydrostatic pressure and $E_{applied}$ in 0.2 mol/L NaOH in the oxidation cell and 0.2 mol/L NaOH + 0.22 g/L thiourea in the hydrogen charging cell at 25 °C.

surface was used in this paper to study the transition state of hydrogen across the surface to the tetrahedral sites of the subsurface [37], since they are more common and representative. In the calculations, 2.832 Å was used as the lattice parameter for bcc Fe. To simulate the diffusion of a single hydrogen atom in the studied structure, a $3 \times 3 \times 3$ super-cell with the (100) surface and k-points sampling of $3 \times 3 \times 1$ were used. To calculate the fractional occupancies, the Brillouin zone sampling was conducted using Monkhorst-Pack scheme [38]. The energy relaxation was continued until the force on each iron atom was below 10^{-4} eV/Å. The adsorption energies of H on Fe (100), which included the one-top sites, two-fold bridge sites and four-fold hollow sites, were calculated, and the four-fold hollow sites had the lowest adsorption energy. The dissolution energies of H in tetrahedral and octahedral sites were obtained, where the dissolution energy in the tetrahedral site is lower than that in the octahedral site for both bcc Fe and subsurface Fe (100). Using the climbing nudged elastic-band (CNEB) tool in the VASP code, the transition state and minimum energy paths between known initial and final positions were obtained [28]. Then, based on the hydrogen diffusion path from the surface adsorption into the Fe (100) subsurface obtained by CNEB, we calculated the Gibbs free energy of each structure at 300 K using the Debye model [29]. Before the Debye model calculations, we calculated the Poisson's ratio in the DFT using the VASP simulations, and found that the Poisson's ratio of bulk Fe was 0.3. The diffusion barrier of Eq. (5) is the energy difference between the transition state and the initial state.

3. Results

3.1. Effect of the hydrostatic pressure on E_{corr}

Potentiodynamic polarization curves were measured on the entry side of each sample under different hydrostatic pressures, as shown in Fig. 1. E_{corr} increases with the hydrostatic pressure. Zhang claimed that E_{corr} of 316 L stainless steel in 3.5% NaCl also increased with the hydrostatic pressure [39]. Sarkar introduced a model based on the Butler–Volmer equation, and the numerical analysis results showed that compressive stress decreased the anodic reaction rate and increased the cathodic reaction rate [40].

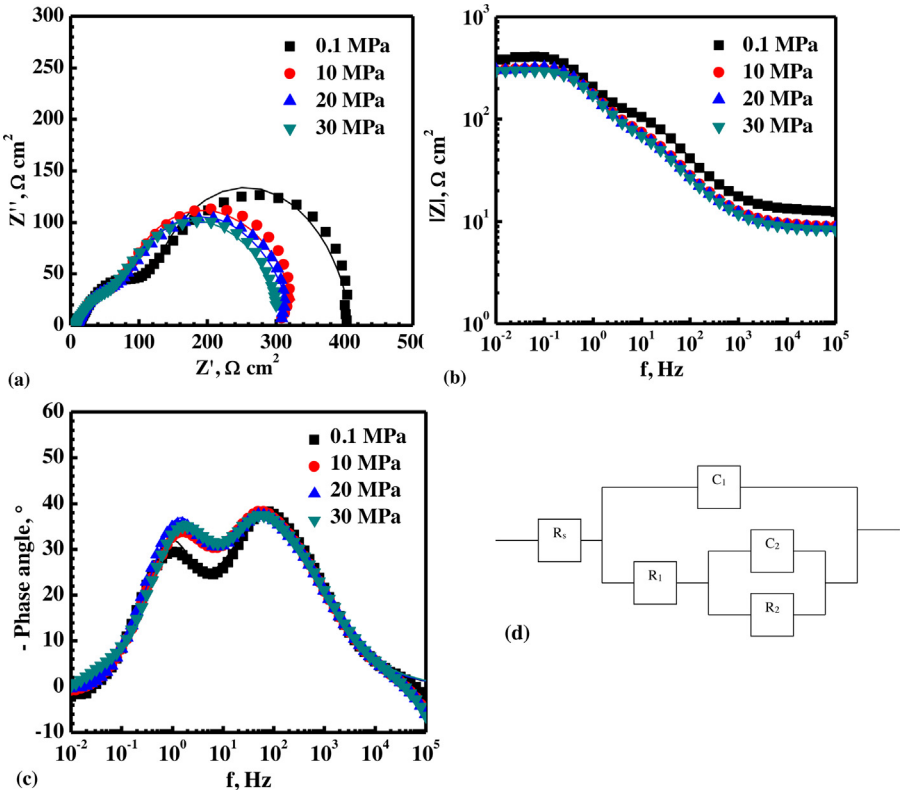

Fig. 4. (a) Impedance spectra in the complex plane for HER on Armco iron in 0.2 mol/L NaOH solution at 25 °C; the applied $E_{applied}$ was −1.06, −1.03, −0.97, and −0.88 V_{SSE} at pressures of 0.1–30 MPa, (the overpotential η with respect to E_{corr} was −0.66 V); (b)-(c) Bode plots for the Armco iron; (d) AHEC equivalent circuit. In (a)-(c), the points denote the experimental data, and the solid lines fit the experimental data with the model in (d).

Table 1
Parameters of the AHEC for HER at Armco iron in 0.2 mol/L NaOH solution under different hydrostatic pressure at 25 °C.

Pressure, MPa	R_1, Ω cm^2	R_2, Ω cm^2	C_1, μFcm^{-2}	C_2, μFcm^{-2}	x_1, Å
0.1	90.25	282.81	37.13	871.31	0.91
10	60.12	239.72	54.31	828.92	0.62
20	55.96	228.71	55.66	795.67	0.60
30	53.59	225.84	55.68	766.33	0.60

The relationship between η and the current in the Tafel linear area is:

$$\eta = -\frac{2.3RT}{(1-\alpha)F}\log j^0 + \frac{2.3RT}{\alpha F}\log j_c \quad (12)$$

Here, j_c is the cathodic current density; j^0 is the exchange current density; α is the transfer coefficient. According to Eq. (12) and Fig. 1, transfer coefficient α is 0.28, 0.32, 0.31, and 0.29 for 0.1–30 MPa, which is independent of the hydrostatic pressure in this experiment. Thus, the mean value of α is 0.3. E_{corr} is −0.40, −0.37, −0.31, −0.22 V_{SSE} under the pressure of 0.1–30 MPa, respectively.

3.2. Hydrogen permeation tests under different hydrostatic pressures

Since E_{corr} increases with the hydrostatic pressure, as shown in Fig. 1, a constant $E_{applied}$ (sum of E_{corr} and preset η) was applied to the hydrogen entry side of the samples to remove the effects of E_{corr}. Thus, the hydrostatic pressure effect on the hydrogen permeation was observed.

Fig. 2 presents the hydrogen permeation curves under different hydrostatic pressures. A series of permeation curves were obtained for the same sample under identical hydrostatic pressures and different $E_{applied}$. The overpotential η with respect to E_{corr} is shown in the brackets in the legend of Fig. 2. Fig. 3 summarizes the data of the steady-state current density i_∞ under different hydrostatic pressures and $E_{applied}$ in Fig. 2. i_∞ continues to increase with the hydrostatic pressure, even if there is no effect of the change in E_{corr}.

3.3. EIS analysis

EIS data were recorded at $E_{applied}$ of −1.06, −1.03, −0.97, and −0.88 V_{SSE} (cathodic overptential of −0.66 V) at the pressures of 0.1, 10, 20, and 30 MPa, as shown in Fig. 4. Fig. 4(a) shows the EIS data for the complex plane, whereas Fig. 4(b) and (c) show the Bode diagrams. Fig. 4(d) shows the Armstrong and Henderson equivalent circuit (AHEC) [41]. The structure of AHEC for HER on the electrode was sufficiently mentioned by Harrington and Conway [42]. In Fig. 4(d), R_s is the resistance of the electrolyte; R_1 is the charge transfer resistance; C_1 is the double-layer capacitance; R_2 is the superficial H_{ad} diffusion resistance; C_2 is the pseudo-capacitance, which is related to the hydrogen diffusion in the bulk metal and HER, based on the Yang's model [43,44]. The Faradaic impedance, Z_f, in the AHEC is:

$$Z_f = R_1 + \frac{R_2}{1 + j\omega\tau_p} \quad (13)$$

Here, ω is the frequency, and $\tau_p = R_2C_2$ is the time constant, which is related to the relaxation rate when the potential changes. The parameters obtained by fitting the results with the AHEC are shown in Table 1. The decrease in R_1 with the hydrostatic pressure demonstrates that the Armco iron electrode has higher charge transport efficiency and increased kinetics of Eq. (1) [45], which indicates that more hydrogen atoms are adsorbed.

3.4. First-principles calculation results

The transition state is represented by hydrogen atom diffusion from the initial position outside the Fe lattice to the tetrahedral site immediately beneath the surface, which was simulated by CNEB. Finally, five positions on the path of hydrogen atom diffusion into the Fe subsurface were selected, and the energy of the system at these positions was calculated with the DFT, as shown in Fig. 5a. Based on the DFT calculation results, the Gibbs free energy of the system was obtained using the Debye model [29], as shown in Fig. 5b. The charge density difference for the five positions on the path of hydrogen atom diffusion is shown in Fig. 6.

4. Discussion

4.1. Change of kinetic parameters of HER vs. hydrostatic pressure

Using the generalized IPZ model, the kinetic parameters of the HER can be obtained. Fig. 7 shows the relationship between the charging function $\sqrt{i_r}/i_\infty i_c \exp(F\alpha\eta/RT)$ and i_∞. The figure shows four straight lines under different hydrostatic pressures with negative slopes and positive intercept according to Eq. (7). Fig. 8 shows a linear relationship between $\ln\left(\sqrt{i_r}/i_\infty\right)$ and i_∞, according to Eq. (8). The linear relationships in Figs. 7 and 8 indicate that HER is tenable only with a coupled discharge-recombination mechanism in the selected potential region [12].

In Eqs. (1) and (2), rate constants k_1 and k_2 are the kinetic diffusion constants. The exchange current density, i_o, hydrogen

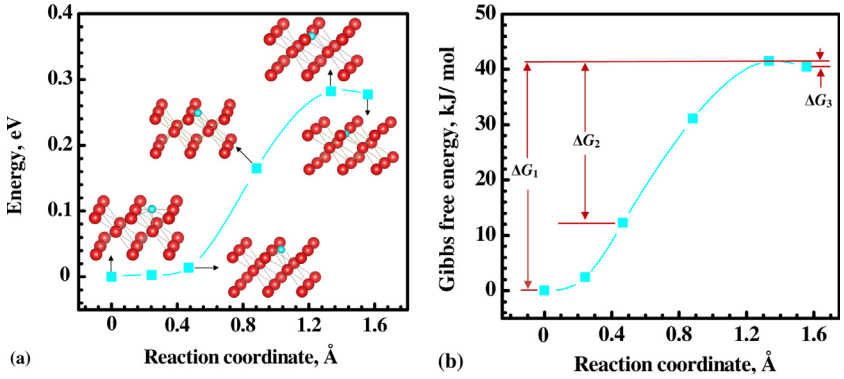

Fig. 5. Minimum energy path for hydrogen diffusion into the Fe subsurface region: (a) DFT calculation results and several intermediate structures along the path; (b) Gibbs free energy of the system from the Debye model.

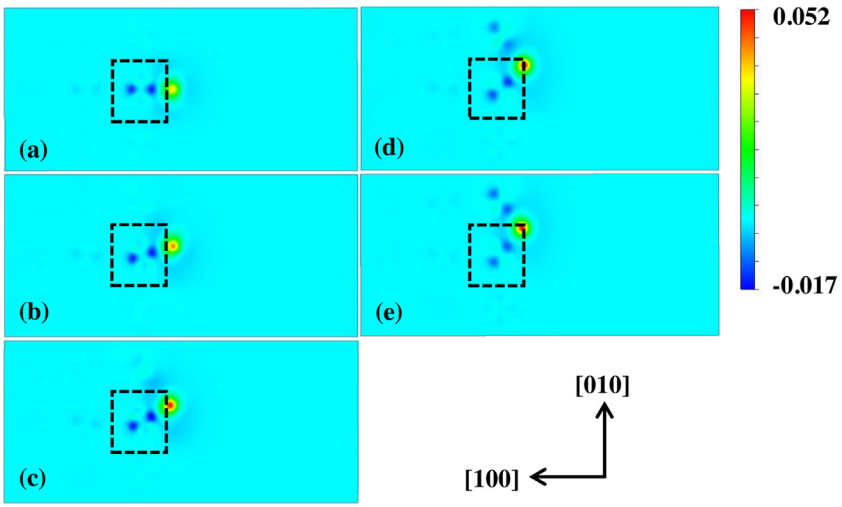

Fig. 6. Charge density difference of the hydrogen atom. (a)-(e) Diffusion of the hydrogen atom from the surface to the tetrahedral site of the subsurface. Each figure corresponds to the marked hydrogen atom position in Fig. 5.

surface coverage θ at the hydrogen entry side, and dimensionless factor, f, were calculated from the data in Figs. 7 and 8 using the generalized IPZ model. The results are summarized in Table 2. According to Table 2, the rate constant k_1 of Eq. (1) increases with the hydrostatic pressure, which indicates that the pressure allows easier adsorption of the ionized hydrogen atoms from H_2O on the sample surface in Eq. (1). Iyer and Pickering demonstrated that the hydrogen charging current density could be written as [14]:

$$i_c = Fk_1^o \exp\left(-\frac{\alpha E_{eq} F}{RT}\right) a_{H_2O} \exp\left(-\frac{\alpha \eta F}{RT}\right)(1-\theta_H) \quad (14)$$

where k_1 is represented by:

$$k_1 = k_1^o \exp\left(-\frac{\alpha E_{eq} F}{RT}\right) \quad (15)$$

Thus, k_1 is related to the equilibrium potential, E_{eq}, of the hydrogen evolution reaction, and E_{eq} is the equilibrium potential of the overall reactions in Eqs. (1)–(3). According to the Nernst equation, E_{eq} is written as:

$$E_{eq} = E_0 + \frac{RT}{2F} \ln \frac{1}{a_{OH^-}^2 P_{H_2}} \quad (16)$$

Since the hydrogen solubility increases with the hydrostatic pressure, hydrogen produced in Eq. (2) dissolves in the solution and gathers at the hydrogen entry side of the sample. P_{H_2} increases with the hydrostatic pressure, whereas E_{eq} decreases with increasing P_{H_2}, and k_1 increases with E_{eq}.

The rate constant k_2 of Eq. (2) decreases with the hydrostatic pressure. The hydrogen solution increases and restrains adsorbed hydrogen atoms from recombining into hydrogen molecules, and k_2 decreases with the hydrostatic pressure. Based on Eq. (9), k is composed of k_{abs}, k_{des}, D, and L. k_{des} is measured to be 1–3×10^{-2} cm s^{-1} in solutions of pH 13 using high-purity iron samples with 50–900 μm thickness [46]. The hydrogen diffusivity in fully annealed and commercially pure iron at 298 K is 4×10^{-5} cm^{-2} s^{-1}, as provided by Zhang [8]. When D and L remain constant,

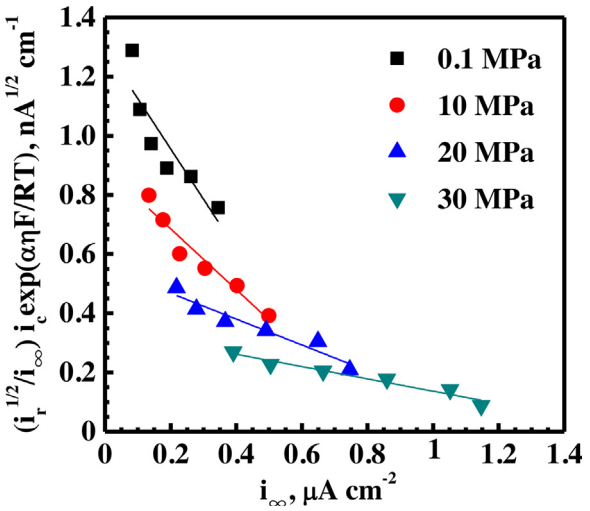

Fig. 7. Relationship between $\sqrt{i_r}/i_\infty i_c \exp(F\alpha\eta/RT)$ and the steady-state hydrogen permeation current density, i_∞. The points are the experimental data, and the solid lines fit the experimental data with Eq. (7).

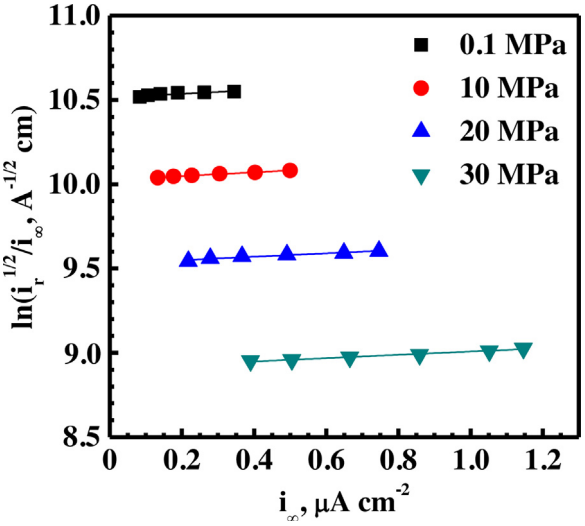

Fig. 8. Relationship between $\ln\left(\sqrt{i_r}/i_\infty\right)$ and the steady-state hydrogen permeation current density, i_∞. The points denote the experimental data, and the solid lines fit the experimental data with Eq. (8).

Table 2
Values of different constants obtained by applying the generalized IPZ analyses to measured steady-state permeation data under different hydrostatic pressure in 0.2 mol/L NaOH in the oxidation cell and 0.2 mol/L NaOH + 0.22 g/L thiourea in the hydrogen charging cell solution at 25 °C.

Pressure	k, 10^{-11} mol cm^{-2} s^{-1}	k_1, 10^{-3} cm s^{-1}	k_2, 10^{-9} mol cm^{-2} s^{-1}
0.1 MPa	0.79	7.32	8.09
10 MPa	0.89	8.21	3.91
20 MPa	1.32	8.58	3.01
30 MPa	1.72	9.65	1.56

increasing k increases k_{abs}/k_{des}. Thus, Eq. (4) moves to the right when the hydrostatic pressure increases. Hydrogen coverage θ at the sample surface is shown in Fig. 9 and increases with the hydrostatic pressure.

As emphasized in previous studies, the hydrogen surface concentration increases with the hydrostatic pressure during galvanostatic hydrogen charging, which is represented by the θ value without the effect of the change in E_{corr}. Thus, the hydrostatic pressure increases the hydrogen surface coverage in two main manners. First, the hydrostatic pressure increases E_{corr}. Thus, the absolute value of the overpotential η increases at the identical $E_{applied}$ under a relatively higher hydrostatic pressure. According to Eq. (14) from Iyer and Pickering [14], the hydrogen charging current density, i_c, increases with the absolute value of η, which increases the value of θ and subsurface hydrogen concentration. Second, the hydrostatic pressure induces the adsorption of hydrogen atoms, which are ionized from H_2O, on the sample surface. However, the hydrostatic pressure increases the solubility of hydrogen molecules and restrains the adsorbed hydrogen atoms from recombining into hydrogen molecules.

4.2. Hydrostatic pressure effect on the double-layer capacitance

The double-layer capacitance, C_1, increases with the hydrostatic pressure, as shown in Table 1. The double-layer capacitance in HER was not fully discussed in the EIS analysis of earlier work, where most researchers considered it with respect to the sample surface roughness [19,21]. Bockris et al. introduced the double-layer capacitance model to describe the electrolyte/solid interface, which is known as the Bockris-Davanathan-Muller (BDM) model [47]. The BDM model was widely used to describe the fixed layer of the double-layer capacitance. Considering the electrolyte concentration and $E_{applied}$ in the experiment, one can reasonably assume that the hydrostatic pressure mainly affects the fixed layer, but not the diffuse layer. Thus, C_1 can be described by Eq. (17) according to the BDM model:

$$\frac{1}{C_1} = \frac{x_1}{\varepsilon_0 \varepsilon_{H_2O}} + \frac{x_2}{\varepsilon_0 \varepsilon_+} \tag{17}$$

Here, x_1 is the thickness of the water molecule dipole layer; x_2 is the distance between the water molecule dipole layer and the outer Helmholtz plane (OHP); ε_0 is the permittivity of vacuum; $\varepsilon_{H_2O}$is the permittivity of water; $\varepsilon_+$is the permittivity of the electrolyte between the water molecule dipole layer and the OHP. Since normally $\varepsilon_{H_2O} \leq \varepsilon_+$, Eq. (17) can be simplified as:

$$\frac{1}{C_1} = \frac{x_1}{\varepsilon_0 \varepsilon_{H_2O}} \tag{18}$$

Dunn et al. have claimed that ε_{H_2O} increases with the hydrostatic pressure at 25 °C [48]. ε_{H_2O}increases from 78.3 to 80.1 in the 0.1–50 MPa pressure range. However, Teschke showed that ε_{H_2O} dramatically increased from 3.8 to 79 at 40 nm from the electrode surface to the electrolyte bulk [49]. ε_{H_2O}can be considered dependent on the distance from the electrode surface, but not on the hydrostatic pressure. It can be 3.8 in the water molecule dipole layer. Combined with Eq. (18), x_1 can be obtained, and the results in Table 1 show that x_1 decreases with the hydrostatic pressure. Thus, the ionized hydrogen atoms remain closer to the electrode surface.

The pressure effect on C_1 is not a linear relationship, which implies that the minimum thickness limit of approximately 0.6 Å for the double-layer capacitance was obtained under 20 MPa pressure. This result agrees with the Shapovalov's research results [21]. The effect of the double-layer structure changes with the initial position of adsorbed hydrogen atoms, as schematically shown in Fig. 10.

The hydrostatic pressure decreases the thickness of the water molecule dipole layer, which makes hydrogen atoms ionized from water near the surface of the Fe lattice. As shown in Fig. 5b, the

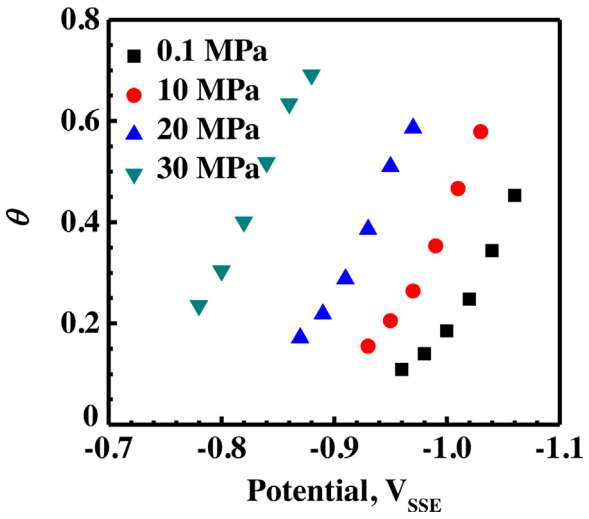

Fig. 9. Relationship among the hydrogen coverage, θ, hydrostatic pressure and $E_{applied}$ in 0.2 mol/L NaOH + 0.22 g/L thiourea solution at 25 °C.

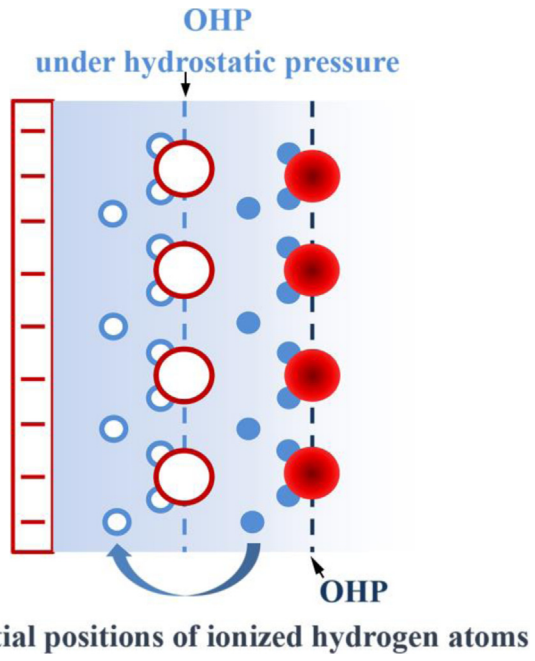

Fig. 10. Effect of the structure change of the double-layer capacitance on the initial position of adsorbed hydrogen atoms at different hydrostatic pressures.

Gibbs free energy of the barrier hydrogen atoms that have diffused from the surface to the subsurface is ΔG_1 under atmospheric pressure, whereas the energy barrier decreases to ΔG_2 when the hydrogen atoms approache the surface under relatively high pressures. Thus, hydrogen atoms must overcome a relatively small energy barrier at higher hydrostatic pressures. According to the Arrhenius equation, k_{abs} and k_{des} can be written as:

$$k_{abs} = A\exp\left(-\frac{\Delta G_{abs}}{RT}\right) \tag{19}$$

$$k_{des} = A\exp\left(-\frac{\Delta G_{des}}{RT}\right) \tag{20}$$

Here, A and B are the pre-exponential factors; R and T have their usual meanings; ΔG_{abs} and ΔG_{des} are the forward and reverse reaction energy barriers in Eq. (4), respectively. Thus, k_{abs} increases with the decrease in ΔG_{abs} from ΔG_1 to ΔG_2, when the hydrogen atoms approach the surface at relatively high pressures. However, k_{des} remains constant at different hydrostatic pressures. Based on Eq. (12), k increases with hydrostatic pressure, which is a physical explanation for the increase in kinetic parameter k with hydrostatic pressure in Table 2.

5. Conclusions

The hydrostatic pressure increased the hydrogen surface coverage in several manners. First, the hydrostatic pressure increased E_{corr}. Second, the hydrostatic pressure made hydrogen atoms more easily ionized from H_2O and subsequently adsorbed on the sample surface. Thus, hydrogen coverage θ at the sample surface increased with hydrostatic pressure. Third, the hydrostatic pressure increased the solubility of hydrogen molecules and restrained the adsorbed hydrogen atoms from recombining into hydrogen molecules.

The EIS results also showed that under relatively high pressures, the OHP was positioned closer to the sample surface, which implied that the adsorbed hydrogen atoms were closer to the sample surface. Based on the DFT and the Debye models calculation results, the closer position induced easier hydrogen atom diffusion from the surface to the tetrahedral sites of the subsurface.

Acknowledgements

This project was supported by the National Natural Science Foundation of China under grant No. 51371035 and the National Basic Research Program of China under grant No. 2014CB643301. AV acknowledges support from the National Science Foundation under the IRES 1358088 grant.

References

[1] T.S. Taylor, T. Pendlington, R. Bird, Foinaven super duplex materials cracking investigation, Offshore Technology Conference, Houston, Texas, 1999, pp. 10965.
[2] S. Olsen, S.M. Hesjevik, Hydrogen embrittlement from CP on supermartensitic stainless steels – recommendations for new qualification methods, Corrosion (2004) 04546.
[3] J. Woodward, R.P.M. Procter, The effect of hydrostatic pressure on hydrogen permeation and embrittlement of structural steels in seawater, Conference Proceedings (1996) 253–267.
[4] L. Nanis Leonard, J.J. DeLuccia, Effects of hydrostatic pressures on electrolytic hydrogen in iron, ASTM STP 445 (1969) 55–67.
[5] A. Smirnova, R. Johnsen, Influence of temperature and hydrostatic pressure on hydrogen diffusivity and permeability in 13% Cr super martensitic stainless steel under cathodic protection, Corrosion 10292 (2010).
[6] R.F. Blundy, L.L. Shreir, Permeation of hydrogen through Fe during cathodic polarization under hydrostatic pressure, Philos. Mag. 20 (1969) 1177–1187.
[7] R.F. Blundy, L.L. Shreir, The effect of pressure on the permeation of hydrogen through steel, Corros. Sci. 17 (1977) 509–527.
[8] T.Y. Zhang, Y.P. Zheng, Effects of absorption and desorption on hydrogen permeation—I. Theoretical modeling and room temperature verification, Acta Mater. 46 (1998) 5023–5033.
[9] X.L. Xiong, X. Tao, Q.J. Zhou, J.X. Li, A.A. Volinsky, Y.J. Su, Hydrostatic pressure effects on hydrogen permeation in A514 steel during galvanostatic hydrogen charging, Corros. Sci. 112 (2016) 86–93.
[10] C. Lim, S.-I. Pyun, Theoretical approach to faradaic admittance of hydrogen absorption reaction on metal membrane electrode, Electrochim. Acta 38 (1993) 2645–2652.
[11] C. Montella, Review and theoretical analysis of ac–av methods for the investigation of hydrogen insertion I. Diffusion formalism, J. Electroanal. Chem 462 (1999) 73–87.
[12] J.O.M. Bockris, J. McBreena, L. Nanis, The hydrogen evolution kinetics and hydrogen entry into α-iron, J. Electrochem. Soc. 112 (1965) 1025–1031.
[13] C. Gabrielli, G. Maurin, L. Mirkova, H. Perrot, B. Tribollet, Transfer function analysis of hydrogen permeation through a metallic membrane in a Devanathan cell. I. Theory, J. Electroanal. Chem. 590 (2006) 1–14.
[14] R.N. Iyer, H.W. Pickering, Analysis of hydrogen evolution and entry into metals for the discharge-recombination process, J. Electrochem. Soc. 136 (1989) 2463–2470.
[15] R.N. Iyer, H.W. Pickering, Construction of iso-coverage tafel plots to evaluate the her transfer coefficient, J. Electrochem. Soc. 137 (1990) 3512–3514.
[16] R.N. Iyer, H.W. Pickering, Mechanism and kinetics of electrochemical hydrogen entry and degradation of metallic systems, Mater. Sci. 20 (1990) 299–338.
[17] F.M. Al-Faqeer, H.W. Pickering, An analysis procedure for hydrogen absorption under frumkin adsorption conditions, J. Electrochem. Soc. 148 (2001) 248–251.
[18] G.M. Sur, La constitution de la charge électrique à la surface d'un électrolyte, J. Phys. Theor. Appl. 9 (1910).
[19] D.L. Chapman, LI. A contribution to the theory of electrocapillarity, Philos. Mag. 25 (1913) 475–481.
[20] O. Stern, Zur theorie der elektrolytischen doppelschicht, Berichte der Bunsengesellschaft für physikalische Chemie 30 (1924) 508–516.
[21] V.L. Shapovalov, The interaction of electric field and hydrostatic pressure in an electrical double layer: A simple first principle model that accounts for the finite sizes of counterions, J. Colloid. Interf. Sci. 454 (2015) 187–191.
[22] W. Dreyer, C. Guhlke, M. Landstorfer, A mixture theory of electrolytes containing solvation effects, Electrochem. Commun. 43 (2014) 75–78.
[23] X. Li, C. Gao, X.L. Xiong, Y. Bai, Y.J. Su, Hydrogen diffusion in α-Fe under an applied 3-axis strain: A quantum manifestation, Int. J. Hydrogen. Energ. 40 (2015) 10340–10345.
[24] P. Kamakoti, D.S. Sholl, A comparison of hydrogen diffusivities in Pd and CuPd alloys using density functional theory, J. Membrane. Sci. 225 (2003) 145–154.
[25] B. Bhatia, D.S. Sholl, Quantitative assessment of hydrogen diffusion by activated hopping and quantum tunneling in ordered intermetallics, Phys. Rev. B. 72 (2005) 224302.
[26] D.E. Jiang, E.A. Carter, Diffusion of interstitial hydrogen into and through bcc Fe from first principles, Phys. Rev. B. 70 (2004) 064102.
[27] D.F. Johnson, E.A. Carter, First-principles assessment of hydrogen absorption into FeAl and Fe3Si: Towards prevention of steel embrittlement, Acta Mater. 58 (2010) 638–648.
[28] D. Sheppard, R. Terrell, G. Henkelman, Optimization methods for finding minimum energy paths, J. Chem. Phys. 128 (2008) 134106.
[29] M.A. Blanco, E. Francisco, V. Luaña, GIBBS: isothermal-isobaric thermodynamics of solids from energy curves using a quasi-harmonic Debye model, Comput. Phys. Commun. 158 (2004) 57–72.
[30] J. Svoboda, F.D. Fischer, Modelling for hydrogen diffusion in metals with traps revisited, Acta Mater. 60 (2012) 1211–1220.
[31] J. Svoboda, G. Mori, A. Prethaler, F.D. Fischer, Determination of trapping parameters and the chemical diffusion coefficient from hydrogen permeation experiments, Corros. Sci. 82 (2014) 93–100.
[32] E. Dabah, V. Lisitsyn, D. Eliezer, Performance of hydrogen trapping and phase transformation in hydrogenated duplex stainless steels, Mat. Sci. Eng. A 527 (2010) 4851–4857.
[33] S. Frappart, A. Oudriss, X. Feaugas, J. Creus, J. Bouhattate, F. Thébault, L. Delattre, H. Marchebois, Hydrogen trapping in martensitic steel investigated using electrochemical permeation and thermal desorption spectroscopy, Scripta Mater. 65 (2011) 859–862.
[34] T. Zakroczymski, Adaptation of the electrochemical permeation technique for studying entry, transport and trapping of hydrogen in metals, Electrochim. Acta 51 (2006) 2261–2266.
[35] G. Kresse, J. Hafner, Ab initio molecular dynamics for liquid metals, Phys. Rev. B. 47 (1993) 558–561.
[36] G. Kresse, J. Furthmüller, Efficiency of ab-initio total energy calculations for metals and semiconductors using a plane-wave basis set, Comp. Mater. Sci. 6 (1996) 15–50.
[37] Y. Yao, L.J. Qiao, A.A. Volinsky, Hydrogen effects on stainless steel passive film fracture studied by nanoindentation, Corros. Sci. 53 (2011) 2679–2683.
[38] H.J. Monkhorst, J.D. Pack, Special points for Brillouin-zone integrations, Phys. Rev. B. 13 (1976) 5188–5192.
[39] C. Zhang, Z.-W. Zhang, L. Liu, Degradation in pitting resistance of 316L stainless steel under hydrostatic pressure, Electrochim. Acta 210 (2016) 401–406.
[40] Y. Ogata, T. Sakka, M. Iwasaki, Diffusion through a multilayered phase in electrochemical systems: an approach by numerical inversion of the Laplace transform, J. Appl. Electrochem. 25 (1995) 41–47.

[41] R.D. Armstrong, M. Henderson, Impedance plane display of a reaction with an adsorbed intermediate, J. Electroanal. Chem. 39 (1972) 81–90.
[42] L. Bai, D.A. Harrington, B.E. Conway, Behavior of overpotential—deposited species in Faradaic reactions—II. ac Impedance measurements on H_2 evolution kinetics at activated and unactivated Pt cathodes, Electrochim. Acta 32 (1987) 1713–1731.
[43] T.-H. Yang, S.-I. Pyun, An investigation of the hydrogen absorption reaction into and the hydrogen evolution reaction from, a Pd foil electrode, J. Electroanal. Chem. 414 (1996) 127–133.
[44] T.-H. Yang, S.-I. Pyun, Hydrogen absorption and diffusion into and in palladium: ac-impedance analysis under impermeable boundary conditions, Electrochim. Acta 41 (1996) 843–848.
[45] M.-R. Gao, J.-X. Liang, Y.-R. Zheng, Y.-F. Xu, J. Jiang, Q. Gao, J. Li, S.-H. Yu, An efficient molybdenum disulfide/cobalt diselenide hybrid catalyst for electrochemical hydrogen generation, Nat. Commun. 6 (2015) 1–7.
[46] M.H.A. Elhamid, B.G. Ateya, H.W. Pickering, Determination of the rate constants of hydrogen absorption into metals, J. Electrochem. Soc. 147 (2000) 2959–2963.
[47] J.O.M. Bockris, M.A.V. Devanathan, K. Muller, On the structure of charged interfaces, P. Roy. Soc. A-Math. Phy. 274 (1963) 55–79.
[48] L.A. Dunn, R.H. Stokes, Pressure and temperature dependence of the electrical permittivities of formamide and water, Trans. Faraday Soc 65 (1969) 6.
[49] O. Teschke, G. Ceotto, E.F. de Souza, Interfacial water dielectric-permittivity −profile measurements using atomic force microscopy, Phys. Rev. E. 64 (2001) 011605.